Title

Deriving cloud velocity from an array of solar radiation measurements

Journal

Solar Energy, 87

ISSN

0038092X

Authors

Bosch, J.L.
Zheng, Y.
Kleissl, J.

Publication Date

2013

DOI

10.1016/j.solener.2012.10.020

Peer reviewed

Deriving cloud velocity from an array of solar radiation measurements

J.L. Bosch, Y. Zheng, J. Kleissl*

Department of Mechanical and Aerospace Engineering
Center for Renewable Resources and Integration
University of California, San Diego
La Jolla, California 92093-0411

Abstract

Spatio-temporal variability of solar radiation is the main cause of fluctuating photovoltaic power feed-in to the grid. Clouds are the dominant source of such variability and their velocity is a principal input to most short-term forecast and variability models. Two methods are presented to estimate cloud speed using radiometric measurements from 8 global horizontal irradiance sensors at the UC San Diego Solar Energy test bed. The first method assigns the wind direction to the direction of the pair of sensors that exhibits the largest cross-correlation in the irradiance timeseries. This method is considered the ground truth. The second method requires only a sensor triplet; cloud speed and the angle of the cloud front are determined from the time delays in two cloud front arrivals at the sensors. Our analysis showed good agreement between both methods and nearby METAR and radiosonde observations. Both methods require high variability in the input radiation as provided only in partly cloudy skies.

Keywords: solar forecasting, solar radiation, cloud motion detection

1. Introduction

The key barrier against high PV penetration scenario is power output variability. Clouds cause spatio-temporal variability of solar radiation that is

*Corresponding Author. Tel.: (858)5348087; Fax: (858)5347599.
E-mail Address: jkleissl@ucsd.edu

the main cause of fluctuating photovoltaic power feed-in to the grid (e.g. Pelland et al. (2011)). Cloud velocity is a principal input to most short-term forecast and variability models (Chow et al. (2011); Hoff and Perez (2010)). For example, a simple estimate for the maximum possible ramp rate of a solar power plant is $dP/dt = P_{csk}k_t v/l$, where P_{csk} is the clear sky power output, k_t is the cloud clear sky index (related to its optical depth), v is the cloud velocity, and l is the length of the power plant in the direction of cloud motion. In words, the ramp magnitude depends on the k_t; in addition the ramp rate is a function of how long it takes for a cloud to cover the plant (assuming that the cloud is larger than the plant). Short term forecasts often rely on advection of a frozen cloud field (Chow et al. (2011); Perez et al. (2010)) using cloud motion vectors (CMVs).

The most common data source to estimate CMVs is satellite imagery (Hammer et al. (1999); Leese et al. (1971); Lorenz et al. (2004)). An early automated technique to obtain CMVs was presented by Leese et al. (1971). Assuming cloud features do not change significantly over a short time interval, a CMV can be computed by locating a feature in successive images. Hammer et al. (1999) developed a statistical method based on conditional probabilities to compute CMVs and predict solar radiation up to 2 hours. Lorenz et al. (2004) used a similar method that minimizes the mean square pixel differences and forecast solar radiation up to 6 hours. Bedka and Mecikalski (2005) improved the Velden et al. algorithm to derive CMVs including both synoptic-scale and mesoscale flows.

Non-linearities in atmospheric motion and cloud formation and evaporation cause Numerical Weather Prediction (NWP) models to outperform satellite-based CMV forecasts for longer forecast time horizons. Perez et al. (2010) and Lorenz et al. (2011) found that, based on the root mean square error (RMSE) metric and point forecasts, on average NWP becomes more accurate than satellite CMVs after 6 hours, which Miller et al. (2011) attributed to the required spin-up time for NWP. For 1 h forecasts, satellite forecasts based on CMVs were only as accurate as persistence forecasts, probably due to satellite navigation and parallax uncertainties (Perez et al. (2010)).

Not only are satellite data complex to acquire and process, but infrequent data update (every 15 to 30 min) and data transfer delays also may not allow detection of mesoscale convective clouds in a timely manner. There also can be a significant difference in the CMV determined from the mesoscale cloud field by the satellite and the speed of individual clouds (Perez, 2012, personal communication). Consequently, local ground measurements of cloud speed

are advantageous for short-term solar variability and solar forecasting.

Different methods have been proposed or used to obtain the cloud speed from ground point sensors. Baldwin and Collins (2011) proposed a network of two concentric circles of sensors around a PV power plant for early cloud detection and cloud speed measurements, but no algorithm to compute cloud speeds was included. Hammer and Stolzenburg (1993) deployed a sensor network across a few buildings and analysed the signal cross-correlations to obtain cloud speed and direction; however, a large number of distributed sensors were required and cross-correlation results needed to be evaluted manually (an automated method was not successful). Similarly, Hinkelman et al. (2011) determined cloud speed by analyzing the lag in the maximum cross-correlation between sensors aligned with the cloud direction, but the method also cannot be automated since cloud direction has to be known a priori.

The main goal in this study is to design a sensor array and automated algorithm to estimate CMV using time delays in cloud arrival times estimated using ground-based pyranometers. In Section 2 the data are described. Section 3 presents two methods for measurements of CMVs. In Section 4 the results from applying these methods on three days are presented and conclusions are provided in Section 5.

2. Data

Global Horizontal Irradiance (GHI) was measured using 8 photodiode pyranometers (Li-200SZ, Licor, Inc.) and logged to a single CR1000 (Campbell Scientific Inc.) datalogger with an acquisition frequency of 20 Hz (Table 1). The sensors were deployed in a semicircular shape with a radius r of 6m as shown in Fig. 1, at the UCSD Solar Energy Test Bed (UCSD-SETB). The sensors were placed onto an exposed rooftop without obstacles or shading and were cross-calibrated on a clear day using linear regression fits.

From MCAS Miramar (KNKX) located 10 km south-east we obtained radiosonde data from the Integrated Global Radiosonde Archive (IGRA) (Durre et al. (2006)) including profiles of pressure, wind speed and direction, and relative humidity. Colocated METAR surface weather data was obtained from the National Oceanic and Atmospheric Administration (NOAA) database (NOAA (2012)). Cloud heights were measured by a ceilometer at

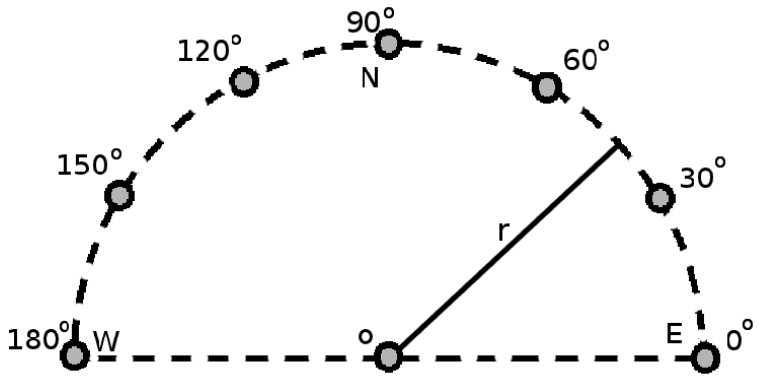

Figure 1: Pyranometer setup showing cardinal direction angles measured counter-clockwise about the origin o and circle radius r.

Table 1: Coordinates and measurement frequency for the utilized databases.

Dataset	UCSD	IGRA	METAR
Lat. [^{o}]	32.885	32.867	32.867
Lon. [^{o}]	-117.240	-117.150	-117.150
Alt. [m]	131	146	146
Sampling	0.05 s	12 h	$\sim$1 h

Automated Surface Observation Station (ASOS). Table 1 shows the main characteristics of the different data sets.

3. Methods

Two different methods to determine CMVs were developed based on the correlation between the GHI timeseries. Following Hinkelman et al. (2011) and Hammer and Stolzenburg (1993), the basic premise is that the GHI time-series for a pair of sensors aligned with the CMV will be highly correlated, but the correlation is largest if the upwind sensor timeseries is lagged by the travel time of the cloud between the two sensors. Once the lag has been determined, cloud speed can be calculated from the sensor spacing. Since cloud direction is variable several pairs of sensors covering many directions are needed. The direction of cloud motion is then given by the alignment of

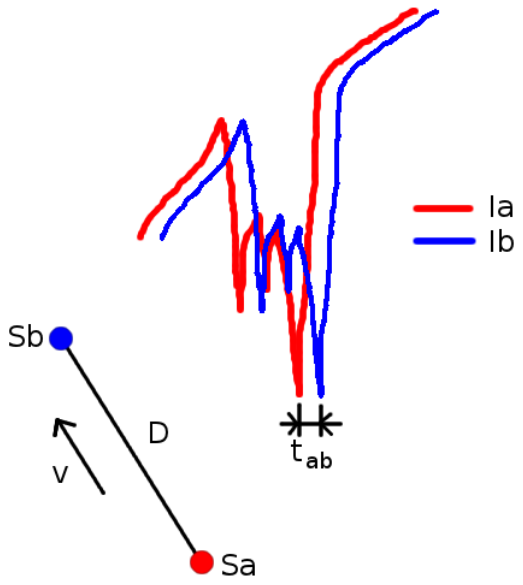

Figure 2: Sample sensor pair with spacing D aligned in the cloud motion direction and irradiance timeseries I_A and I_B.

the most correlated pair. An alternative method to calculate CMV is proposed using a reduced set of three sensors. However, in this case the angle of the cloud shadow edge relative to the array also has to be determined.

3.1. Most Correlated Pair Method (MCP)

The basic premise is that for a pair of sensors S_a and S_b aligned with the cloud motion, separated by a distance D, the irradiances I_a and I_b are highly correlated, but with a time lag t_{ab} (Fig. 2). Once the lag has been determined (e.g. by analyzing the signal cross correlation), cloud speed can be calculated as

$$v = D/t_{ab} \tag{1}$$

For the experiment, 8 sensors are grouped in 7 pairs, where all pairs share the central sensor. The cross correlation was performed for all 7 pairs with a timestep of 5s, and using a time window of 30s (600 data points). The pair with the largest cross correlation coefficient $\rho(t_{ab})$ is assumed to be the most aligned with the CMV. Cloud speed is then calculated using the most

Table 2: Example MCP results for October 20^{th}, 1205PST. Each pair is characterized by their aligment direction θ. Resulting time lag t_{AB} and speed v for the most correlated pair are higlighted.

Pair #	θ [^{o}]	$\rho(t_{AB})$	t_{AB} [s]	v [m s^{-1}]
1	0	0.7140	1.65	3.6
2	30	0.7062	1.70	3.5
3	60	0.7433	1.35	4.4
4	90	0.8123	0.80	7.5
5	**120**	**0.8483**	**1.05**	**5.7**
6	150	0.8268	0.85	7.1
7	180	0.7629	0.30	20

correlated pair according to Eq. 1. Table 2 shows an example of MCP results for 7 pairs of sensors.

With the MCP method there is a tradeoff between the resolution at which the cloud direction can be determined (here for $n = 7$ pairs, $180/(n-1) = 30^o$) and the number of sensors. If more sensors are deployed the cloud direction becomes more accurate. More accurate cloud direction also translates into more accurate cloud speed. For our setup, cloud direction errors of up to $30^o/2 = 15^o$ result in cloud speed errors of up to $1-\cos 15^o = 3.4\%$, which is acceptable. However, in general to obtain errors of less than 5% at least 7 sensors are needed.

Since the MCP method is based on a relatively simple and proven concept it will be used together with the measured METAR and radiosonde data for validation purposes.

3.2. Linear Cloud Edge Method (LCE)

Note that the method is presented conceptually in terms of the passing of a cloud edge, since it is more intuitive. However, the implementation is based on maxima and minima in the irradiance timeseries which will be described near the end of this section. The simple Eq. 1 cannot be applied for a (more readily available) triplet of sensors since the cloud edge is generally not aligned with the axes of the sensor setup. Consequently, the irradiance ramp observed by the sensors is caused by different parts of the cloud front and the cloud speed cannot be determined simply from the time delays of

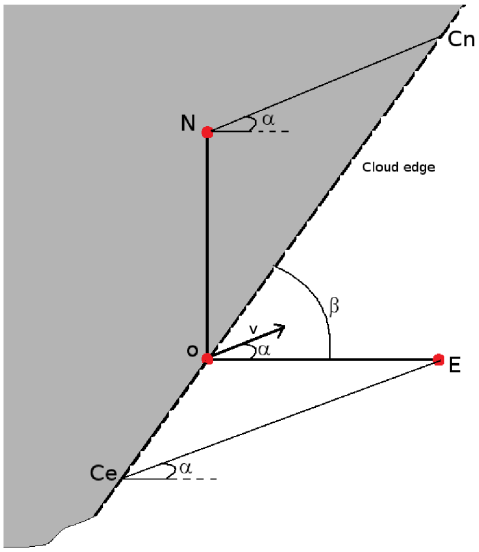

Figure 3: Schematic of a linear cloud edge passing a sensor triplet. β is the angle between the cloud edge and the x axis, and α is the angle between the CMV $\mathbf{v}$ and the x axis. C_e and C_n are the cloud edge points that pass over sensors N and E.

the sensors. The main implication is that maximum cross correlation cannot be applied to this reduced setup. An alternative method is proposed using a triplet of sensors; CMVs are calculated assuming a linear cloud shadow edge (LCE) passing through the array. LCE method uses the sensors labeled as o, E and N in Fig. 1, where the distances $\overline{oN} = \overline{oE} = D = 6$ m (Fig. 3).

We assume (i) a linear cloud edge shape across the sensor array; (ii) constant CMV while passing over the three sensors; (iii) the cloud is large enough to cover all three sensors. For closely spaced sensors of O(10 m), (ii) will always hold. (i) and (iii) are generally satisfied if the sensor spacing $\sim$ 1–10m is small compared to the cloud dimensions $\sim 10^2$–10^3m. We define the time needed for the cloud to move from C_n to N (t_{on}) and from C_e to E (t_{oe}). The cloud motion direction is given by either the lines $\overline{NC_n}$, $\overline{C_eE}$ or the motion vector. Equations 2-11 show the steps to calculate the CMV.

Using the cloud speed v

$$v = [v\cos\alpha, v\sin\alpha], \tag{2}$$

the sensor and cloud edge positions

$$\begin{array}{rcl} r_o & = & [0,0] \\ r_N & = & [0,D] \\ r_E & = & [D,0] \\ r_{C_e} & = & [C_{ex},C_{ey}] \\ r_{C_n} & = & [C_{nx},C_{ny}], \end{array} \tag{3}$$

and the edge equation at the origin

$$\tan\beta = C_{ey}/C_{ex} = C_{ny}/C_{nx}, \tag{4}$$

the following basic kinematic equations

$$\begin{array}{l} r_E - r_{C_e} = t_{oe}v \\ r_{C_n} - r_N = t_{on}v \end{array} \tag{5}$$

can be used to yield the analytic expressions for t_{on} and t_{oe}

$$t_{oe} = -\frac{D\tan\beta}{v(\sin\alpha - \cos\alpha\tan\beta)} \tag{6}$$

$$t_{on} = -\frac{D}{v(-\sin\alpha + \cos\alpha\tan\beta)}. \tag{7}$$

Solving Eqs. 6 and 7 or applying the Law of sines to the triangles oNC_n, and oEC_e yields

$$\beta = \arctan\left[-\frac{t_{oe}}{t_{on}}\right]. \tag{8}$$

Finally, replacing β from Eq. 8 into Eqs. 6-7,

$$t_{on}\sin\alpha + t_{oe}\cos\alpha = D/v. \tag{9}$$

Since the time lags t_{on} and t_{oe} can be obtained from the measurements, we are left with two unknowns (α and v), and one equation (Eq. 9). The additional information needed to solve Eq. 9, can be obtained from a second cloud edge passing through the sensors, with same v and α, but with a different β. Since β can take on any value in $[0,180]$ different t_{on} and t_{oe} will result.

Assigning the indeces 1 and 2 for the first and second pass, respectively, leads to Eq. 10

$$\begin{array}{rcl} t_{on1}\sin\alpha + t_{oe1}\cos\alpha & = & D/v \\ t_{on2}\sin\alpha + t_{oe2}\cos\alpha & = & D/v, \end{array} \tag{10}$$

that can be reduced to

$$\alpha = \arctan\left[-\frac{t_{oe2} - t_{oe1}}{t_{on2} - t_{on1}}\right]. \tag{11}$$

Once α is obtained from Eq. 11, v can be calculated using Eq. 10.

Attempts to determine the time lags from the cross-correlation method or from the timing of the largest ramps (edge overpass) were unsuccessful. Rather t_{oe} and t_{on} are determined from the timing of local maxima and minima of the measured GHI. The maxima can occur when cloud enhancement causes an increase in GHI just before of after a cloud shades the sensors, while minima in GHI occur near the cloud center. More often, localized maxima and minima occur during the shading event due to variability in intra-cloud opacity. Time lags between the maxima and minima observed at different sensor locations yield t_{oe} and t_{on} for particular cloud events.

High data acquisition frequency can lead to noisy signals. Local maxima and minima could then be caused by noise rather than atmospheric effects leading to errors in both the cloud speed and direction. To avoid this and other erroneus maxima and minima detection, preprocessing is conducted. It consists of:

- Moving average: First, data is preprocessed by applying a 5-point (corresponding to 0.25 s) moving average. Applying the moving average had little effect in periods of high irradiation variability, but improved results for lower irradiation variability. Some noisy variability persisted after the smoothing, but this will be addressed in the third step.

- Global maxima: Global maxima over a moving window of 15 s are selected and local maxima are discarded. This step ensures that the cloud-edge-passing events with the largest variability are selected.

- Broad shoulders: From the remaining maxima, only peaks with "broad shoulders" are selected, i.e. those whith three monotonous ascending values before the maxima and three monotonous descending values after the maxima. This step further reduces noise effects.

- Simultaneous peaks: The earlier steps lead to a set of maxima candidates at different times for each sensor, but only near-simultaneous peaks could have been caused by the same cloud edge. The three

maxima obtained by the different sensors are considered to be "simultatenous" if the north and east sensor peaks occur less than 3 seconds before or after the origin sensor peak.

- The three different times for the simultaneous maxima yield the time lags t_{oe} and t_{on} for each event, but two events are needed to obtain the CMV. If two events were too far separated in time, the assumption of constant CMVs may be violated. Consequently, two cloud events are required to occur within 5 min. Generally, a sufficient amount of maxima or minima should be available from a single cloud passage, but the extrema may also come from separate cloud events within the 5 min window.

- The same process is repeated for the minima, producing another set of CMVs which is added to the one obtained from the analyzed maxima. In general minima detection was found to be less robust, so minima and maxima were not mixed and CMVs were determined separately for minima and maxima. For example 461 maxima and 430 minima passed the broad shoulders test for October 20^{th}, leading to 255 and 229 simultaneos maxima and minima respectively (i.e. 484 CMVs). The number of calculated CMVs for a given day will depend on the GHI variability.

3.3. Quality control

Quality control is applied to both the raw MCP and LCE results. Poorly correlated measurements that occur in overcast and clear periods leads to random MCP derived directions as those shown in Fig. 5. While in principal the variability in cloud optical depth in overcast layers should yield MCP results, the correlation obtained from different pairs are so close that random correlations in signal noise dominate. Based on empirical evidence, CMVs are excluded if the maximum cross-correlation coefficient

$$\rho_i \quad < \quad 0.775, \tag{12}$$

where ρ_i is the maximum correlation coefficient for the most correlated pair of sensors at instant i.

Raw LCE results were also highly variable and needed to be quality controlled. The reason is that – even after the preprocessing described in Section 3.2 – GHI maxima and minima were detected that are not related to

cloud passages; however, when there are a sufficient number of cloud passages the LCE method yields consistent results. Unphysical cloud speeds and speed and direction outliers are excluded as follows:

$$\begin{aligned} v_i &> 50\text{ms}^{-1} \\ |v_i - v_{mean}| &> 2v_\sigma \\ |\alpha_i - \alpha_{mean}| &> 2\alpha_\sigma, \end{aligned} \tag{13}$$

where v_i and α_i are the cloud speed and direction calculated at instant i, v_{mean} and α_{mean} are the average calculated speed and direction; and v_σ and α_σ are the standard deviations of the calculated speeds and directions. Mean and the standard deviations are calculated over the preceeding 30 minutes.

4. Results

From a set of 10 days of ground measurements, 4 days were clear or almost clear and 3 days were overcast with small GHI variability for most of the day. For clear and overcast days, cloud speeds are of little value since variability is small and power output is highly predictable. The methods were tested the three remaining days with partial cloud cover, October 20^{th}, 21^{st}, and 25^{th} 2011. Review of total sky images indicated that cumulus was the main type of cloud observed for October 20^{th} and stratocumulus for October 21^{st}, while overcast skies were observed for most of October 25^{th}. METAR reported low cloud heights for October 20^{th} and 21^{st}, in the range [274-640] m, and higher clouds of [1200-1800] m for October 25^{th}. For October 20^{th} clouds were reported to be broken from 8 to 11PST, scattered/few from 11 to 17 PST and then overcast for the rest of the day. For October 21^{st} clouds were reported to be few for most of the day with periods of clear sky and scattered clouds. For October 25^{th} the sky was reported as overcast for most of the day. Fig. 4 shows the two radiosonde profiles for wind direction α and speed v taken on October 20^{th}. The only daytime measurement occurs at 1623 PST, which does not overlap but is only 30 min after the last results for cloud direction were obtained from the MCP and LCE methods. METAR cloud height h at the closest time was used to select the cloud altitude in the radiosonde wind profile. Table 3 shows the measured α and v values at 1623 PST that serve as a reference in the LCE and MCP model validation.

To illustrate the performance of the MCP method, Fig. 5 shows 20 min of data on October 21^{st}. During the first 10 min in clear skies MCP outputs a random direction α in the range [-180,180]. In this interval both the

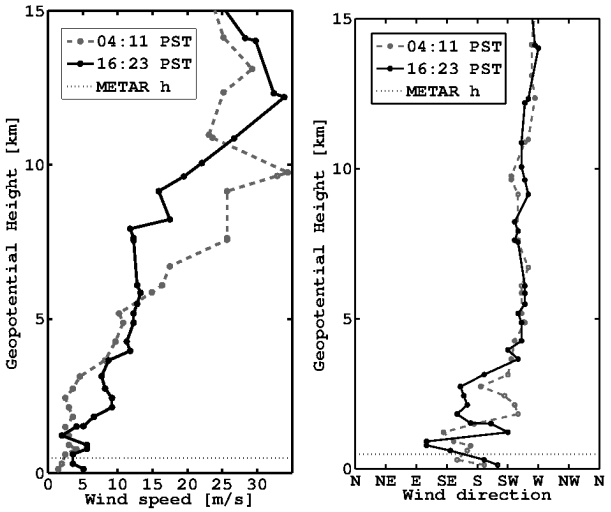

Figure 4: Profiles of radiosonde wind direction and speed on October 20, 2011. The cloud height reported by METAR at KNKX at 1655 PST is shown as a horizontal line.

maximum cross correlation coefficient and the standard deviation of GHI are small. After 12.7 h, α becomes consistent at 30^oSE. Solar irradiance in this second interval shows larger variability and maximum cross correlation coefficient due to cumulus clouds.

Figure 6 shows the results obtained for the study days. For October 20^{th}, both methods fail to extract usable CMVs during the overcast morning. In the interval 1300-1600 PST, both methods produce similar directions, also comparable to the 1623 PST IGRA radiosonde data. Again, for October 21^{st}, small variability in the measured GHI during overcast or clear sky periods causes both MCP and LCE results to fail the quality control, and this is also the reason for the reduced number of points obtained for October 25^{th}. The cloud direction was different for the three study days; both methods reflect the intra and inter-day variability and agree with the radiosonde measurement. The α results also agree with cloud directions determined visually from total sky imagery (movies are provided in the added online content to this paper).

In addition, a self-consistency test was performed on the LCE method by using different (rotated) triplets of sensors from the semicircular shape (i.e. the triplet formed by the origin, 30^o and 120^o sensors). This independent analysis yielded consistent cloud directions (not shown) confirming the

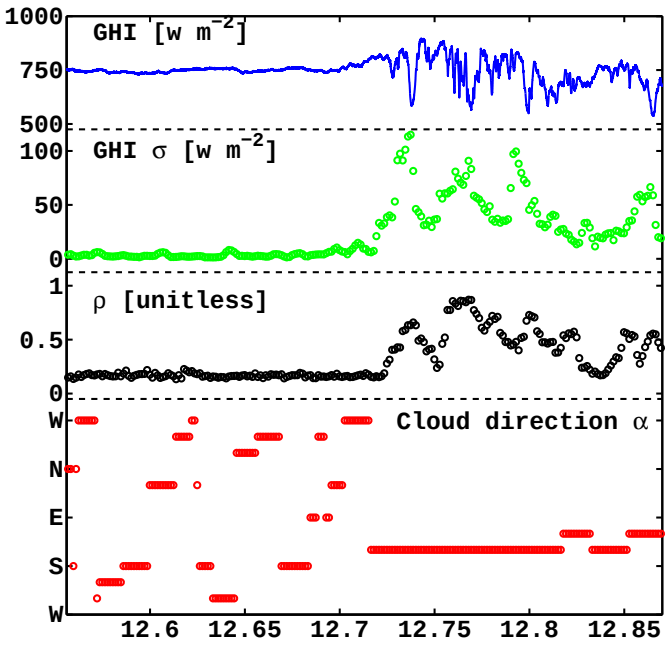

Figure 5: GHI and its standard deviation σ every 5 s over 30 s intervals and MCP results for maximum correlation coefficient ρ and cloud direction α on October 21, 2011.

Table 3: Cloud speed and direction obtained from radiosonde data for the cloud height h observed by METAR (Fig. 4).

Date	Oct 20^{th}	Oct 21^{st}	Oct 25^{th}
PST_{IGRA}	1623	1623	1623
PST_{METAR}	1655	1655	1655
Cloud Type	Scattered	Scattered	Broken
h [m]	457	610	1463
α [^{o}]	165	5	270
v [m s^{-1}]	3.6	2	4.6

robustness of the LCE method.

While cloud direction serves as a point of comparison of the different methods, the primary output relevant to solar power variability is cloud speed. The results confirm those obtained for the cloud direction, with a similar output from both MCP and LCE methods of about 5 m s^{-1} on October 20^{th} and 21^{st} and 5 to 10 m s^{-1} on the 25^{th}, in agreement with radiosonde observations. The LCE results are more variable than the MCP results. The variability could be caused by several factors: (*i*) Resolution of the measurements. With cloud speeds of about 5 m s^{-1} cloud passage takes about 1.2 sec. Consequently, the measurement resolution of 0.05 sec can cause errors of up to 4%. (*ii*) Physical variability in cloud speed due to the flow over topography causing convergence of streamlines and larger velocity gradients with height (the site sits on top of a ridge that slopes about 10% towards the ocean). (*iii*) Clouds are naturally turbulent and may not travel exactly with the speed of the ambient atmosphere.

MCP and LCE results are not temporarily aligned. To objectively analyze the consistency of both methods, 30 min vector averages of speed and direction were compared on the three study days. Figures 7a and 7b show the results for direction and speed, respectively. Linear regression between the LCE α and MCP directions show a regression factor R^2 of 0.977 and a root mean squared error of RMSE=16.5^o. The same regression performed for the speeds resulted in a regression factor R^2 of 0.875 and RMSE=0.40ms^{-1}.

From the LCE method, cloud edge angles β were obtained from Eq. 8 as ancillary products. β is predominantly perpendicular to α (Fig. 8). A similar relationship between the angles would be obtained if circles moved over the

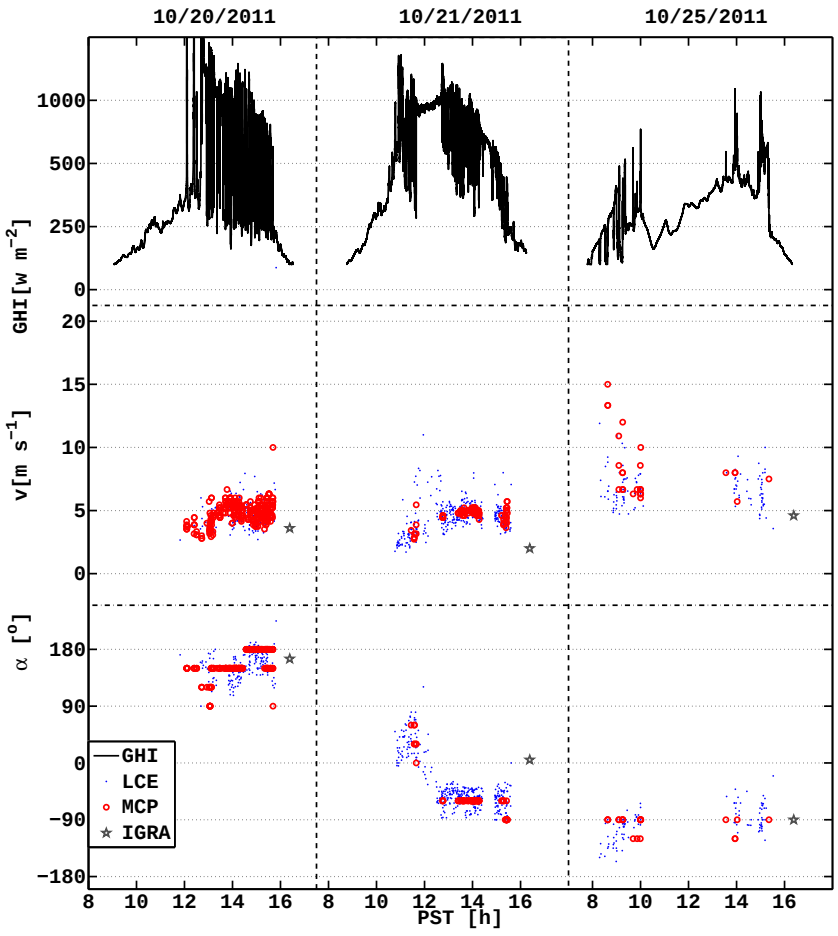

Figure 6: GHI and cloud motion vector comparison for October 20^{th}, 21^{st} and 25^{th}. Radiosonde (IGRA) results obtained at 1623 PST are shown as stars.

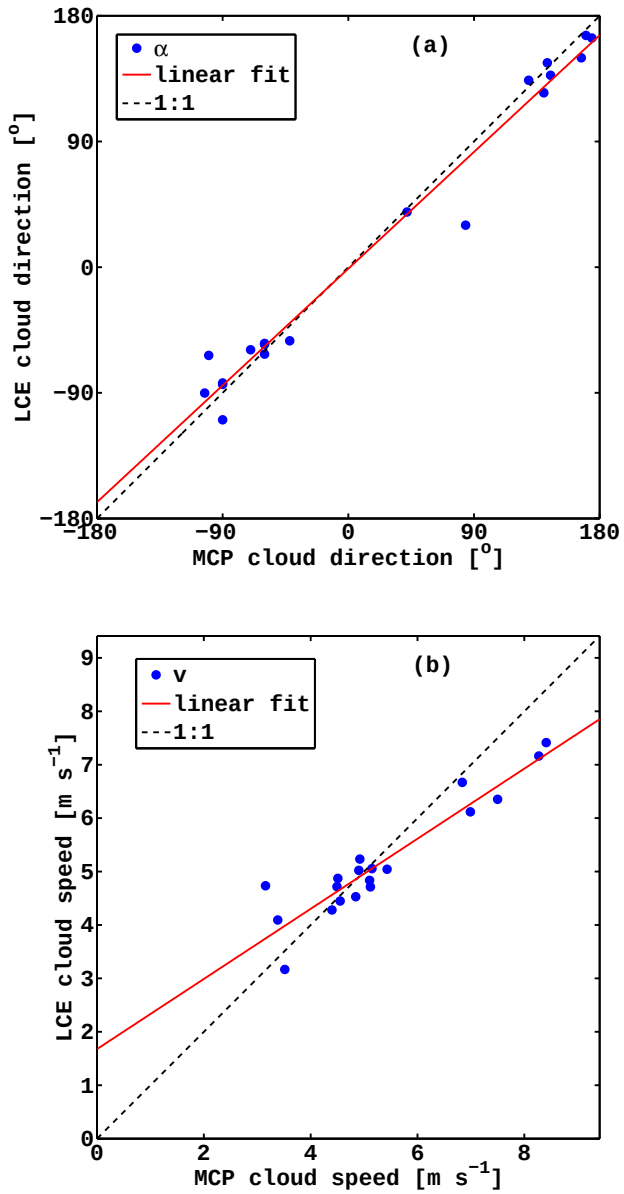

Figure 7: LCE vs MCP half-hourly (a) α and (b) v averages on October 20^{th}, 21^{st}, and 25^{th}, 2011.

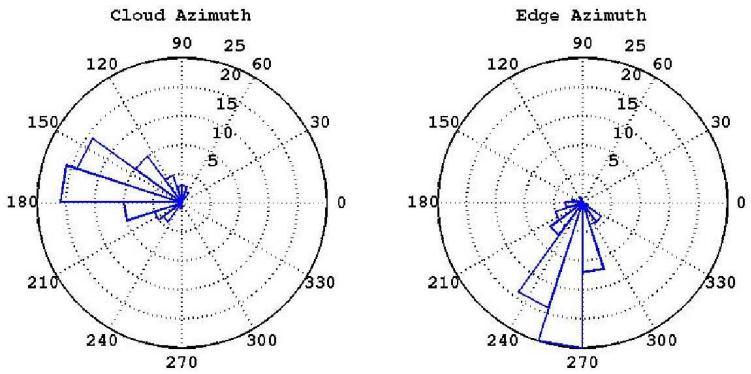

Figure 8: Polar histogram for β and α directions for October 20^{th}.

sensors as then the likelihood of $\beta = \alpha$ would be zero. If β perpendicular to α could be generally assumed, it would allow simplifying the set of equations 4-11 requiring just one cloud pass to derive the CMV. However, instantaneous $\beta - \alpha$ shows a wide distribution centered around 90^o, so our more general method should be applied.

5. Conclusions

Encouraging CMV results are obtained from an array of ground measurements after quality control is conducted. On three days with variable cloud directions and speeds, the CMVs were well characterized by both MCP and LCE methods. Cloud directions from the LCE method were consistent with the more established MCP approach and visual analysis of sky imagery. LCE cloud speeds were similar to MCP speeds and consistent with radiosonde data. The MCP has the advantage of simplicity, robustness, and computational speed. The LCE method is superior in reduced installation and maintenance costs of the sensor array. Both methods require high variability in the radiation from clear-cloudy or cloudy-clear transitions. Cloud speed of an overcast cloud layer or the atmospheric velocity in clear skies cannot be obtained, but there is also little practical relevance at these times. Just like with the satellite CMV approach, the absolute accuracy of the cloud speed method is difficult to ascertain due to the lack of high quality reference measurements.

The MCP is the more robust approach and should be considered the ground truth. However, the LCE showed similar results and is viable as a

low-budget approach whenever the installation/maintenance of a large array of pyranometers is not possible.

Future work will focus on the analysis of different combinations of acquisition frequencies and array sizes, in order to optimize the output from both methods. Also, although completely clear skies will not produce a CMV output, the other low variability case corresponding to completely overcast skies will be further analyzed to improve the methods results in those situations. Finally techniques that enable the detection of two cloud layers will be investigated.

Acknowledgments

This work was supported in part by the California Solar Initiative RD&D program. Jordan Liss assisted with data collection. Facilities personnel (David Purtell and Mildred Mcmilion) at RIMAC Sports Facilities are gratefully acknowledged for hosting the experiment.

References

Baldwin, R.R., Collins, K., 2011. Cloud tracking. U.S. Patent US20110060475.

Bedka, K.M., Mecikalski, J.R., 2005. Application of satellite-derived atmospheric motion vectors for estimating mesoscale flows. Journal of Applied Meteorology 44, 1761–1772.

Chow, C.W., Urquhart, B., Lave, M., Dominguez, A., Kleissl, J., Shields, J., Washom, B., 2011. Intra-hour forecasting with a total sky imager at the UCSan Diego solar energy testbed. Solar Energy 85, 2881–2893.

Durre, I., Vose, R.S., Wuertz, D.B., 2006. Overview of the Integrated Global Radiosonde Archive. Journal of Climate 19, 53–68.

Hammer, A., Heinemann, D., Lorenz, E., Lückehe, B., 1999. Short-term forecasting of solar radiation: a statistical approach using satellite data. Solar Energy 67, 139–150.

Hammer, A., Stolzenburg, K., 1993. Analyse kurzfristiger Fluktuationen der Solarstrahlung unter Berücksichtigung von Wolkenfeldstrukturen. Diploma thesis. Carl von Ossietzky University of Oldenburg. Oldenburg, Germany.

Hinkelman, L., George, R., Wilcox, S., Sengupta, M., 2011. Spatial and temporal variability of incoming solar irradiance at a measurement site in Hawai'i. 91st American Meteorological Society Annual Meeting, January 23 - 27, 2011. Seattle, WA, United States .

Hoff, T.E., Perez, R., 2010. Quantifying PV power output variability. Solar Energy 84, 1782–1793.

Leese, J.A., Novak, C.S., Clark, B.B., 1971. An automated technique for obtaining cloud motion from geosynchronous satellite data using cross correlation. Journal of Applied Meteorology 10, 118–132.

Lorenz, E., Hammer, A., Heinemann, D., 2004. Short term forecasting of solar radiation based on satellite data. Proc. ISES Europe Solar Congress EUROSUN2004,Freiburg, Germany, 2004 .

Lorenz, E., Scheidsteger, T., Hurka, J., Heinemann, D., Kurz, C., 2011. Regional PV power prediction for improved grid integration. Progress in Photovoltaics: Research and Applications 19, 757–771.

Miller, S.D., Combs, C.L., Sengupta, N., Chand, D., Heidinger, A.K., 2011. Toward evaluating short-term predictions of solar irradiance at the surface: persistence, satellite-based trajectory and numerical weather prediction models. Proc. ASES Annual Conf.,Raleigh, NC, 2011 .

NOAA, 2012. http://cdo.ncdc.noaa.gov/qclcd/qclcd. Last time acessed on March.

Pelland, S., Galanis, G., Kallos, G., 2011. Solar and photovoltaic forecasting through post-processing of the Global Environmental Multiscale numerical weather prediction model. Progress in Photovoltaics: Research and Applications Http://dx.doi.org/10.1002/pip.1180.

Perez, R., Kivalov, S., Schlemmer, J., Jr., K.H., Renné, D., Hoff, T.E., 2010. Validation of short and medium term operational solar radiation forecasts in the US. Solar Energy 84, 2161–2172.

Velden, C.S., Olander, T.L., Wanzong, S., 1998. The impact of multispectral goes-8 wind information on atlantic tropical cyclone track forecasts in 1995. part i: Dataset methodology, description, and case analysis. Monthly Weather Review 126, 1202–1218.